# Observations and simulations of receiver-induced refractivity biases in GPS radio occultation

G. Beyerle, T. Schmidt, J. Wickert, S. Heise and M. Rothacher

GeoForschungsZentrum (GFZ) Potsdam, Germany

G. König-Langlo

Alfred Wegener Institute for Polar and Marine Research, Bremerhaven, Germany

K. B. Lauritsen

Danish Meteorological Institute, Copenhagen, Denmark

---

G. Beyerle, GeoForschungsZentrum Potsdam (GFZ), Department 1, Geodesy and Remote Sensing, Telegrafenberg, D-14473 Potsdam, Germany (e-mail: gbeyerle@gfz-potsdam.de)

S. Heise, GeoForschungsZentrum Potsdam (GFZ), Department 1, Geodesy and Remote Sensing, Telegrafenberg, D-14473 Potsdam, Germany (e-mail: stefan.heise@gfz-potsdam.de)

G. König-Langlo, Alfred Wegener Institute for Polar and Marine Research, Bremerhaven, Germany (e-mail: gkoenig@awi-bremerhaven.de)

K. B. Lauritsen, Danish Meteorological Institute, Copenhagen, Denmark (e-mail: kbl@dmi.dk)

M. Rothacher, GeoForschungsZentrum Potsdam (GFZ), Department 1, Geodesy and Remote Sensing, Telegrafenberg, D-14473 Potsdam, Germany (e-mail: rothacher@gfz-potsdam.de)

T. Schmidt, GeoForschungsZentrum Potsdam (GFZ), Department 1, Geodesy and Remote

**Abstract.** An analysis of 206,422 atmospheric refractivity profiles observed by the CHAMP geo-research satellite between 14 May 2001 and 30 June 2005 reveals significant biases compared to ECMWF meteorological fields at altitudes below 5 km. The mean bias decreases down to −2% at altitudes below 2 km; in the Amazon region positive biases exceeding +1% are observed. In order to identify bias contributions caused by the receiver signal tracking process an end-to-end simulation study implementing different signal tracking modes was performed. The end-to-end simulations are based on 1992 radio sonde profiles obtained regularly aboard research vessel "POLARSTERN" since December 1982 and were conducted with four receiver models using closed-loop, fly-wheeling and open-loop signal tracking methods. The simulation results confirm that open-loop tracking yields significantly smaller biases and standard deviations of the fractional refractivity errors compared to fly-wheeling enabled receivers. In addition, we analyze closed-loop tracking with a second order loop and demonstrate that similar reductions in biases and standard deviations can be obtained.

Sensing, Telegrafenberg, D-14473 Potsdam, Germany (e-mail: tschmidt@gfz-potsdam.de)

J. Wickert, GeoForschungsZentrum Potsdam (GFZ), Department 1, Geodesy and Remote Sensing, Telegrafenberg, D-14473 Potsdam, Germany (e-mail: jens.wickert@gfz-potsdam.de)

## 1. Introduction

Since February 2001 a Global Positioning System (GPS) radio occultation (RO) experiment aboard the CHAMP (CHAllenging Minisatellite Payload) geo-research satellite [*Reigber et al.*, 2002, 2005] monitors atmospheric temperature and water vapor with high vertical resolution. The "BlackJack" GPS receiver aboard CHAMP records characteristic signal amplitude and phase changes induced by the ionosphere and neutral atmosphere. From the observed signal phase and amplitude the ray bending angle profile $\alpha(p)$ and subsequently the atmospheric refractivity profile $N(z) = (n(z) - 1) \cdot 10^6$ are derived. Here, $n(z)$ denotes the real part of the atmospheric refractive index, $p$ and $z$ are the ray impact parameter and the altitude, respectively. For the history and detailed accounts of the radio occultation technique see e.g. *Yunck et al.* [2000]; *Melbourne et al.* [1994]; *Kursinski et al.* [1997]; *Hajj et al.* [2002].

Since activation of the RO experiment aboard CHAMP on 11 February 2001 more than three hundred thousand of occultation events have been observed, 64% of which could be successfully processed and converted to profiles of atmospheric temperature [*Wickert et al.*, 2001, 2004; *Hajj et al.*, 2004]. At altitudes between about 7–8 km and 35 km good agreement between RO measurements and meteorological analyses is found. In the lower troposphere, however, CHAMP validation studies consistently report on a negative refractivity bias of several percent [*Wickert et al.*, 2004; *Marquardt et al.*, 2003; *Ao et al.*, 2003; *Hajj et al.*, 2004]. This negative $N$-bias is well known from the proof-of-concept GPS/MET mission and was first described by *Rocken et al.* [1997] within the GPS/MET data validation study.

The $N$-bias may be attributed to two factors. First, for vertical refractivity gradients below a threshold value of $dN_c/dz \equiv 10^6/r_E \approx -157$ km$^{-1}$ the ray's local radius of curvature falls below $r_E$, Earth's local radius of curvature. Ray tangent points within the critical layer are inaccessible using a RO geometry with the transmitters located above the layer [*Ao et al.*, 2003; *Sokolovskiy*, 2003, 2004]. In occultation events affected by critical refraction the retrieved bending angles and, subsequently, the retrieved refractivities are systematically smaller than the true values [*Sokolovskiy*, 2004]. Second, the signal tracking process performed by the occultation receiver may induce carrier phase errors which also contribute to the refractivity bias [see e.g., *Gorbunov*, 2002; *Ao et al.*, 2003; *Beyerle et al.*, 2003].

Closed-loop receivers track the incoming GPS carrier signal by correlating it with a model signal generated by a numerically-controlled oscillator (NCO) [*Kaplan*, 1996; *Misra and Enge*, 2002]. The NCO's frequency, in turn, is steered towards the incoming signal's frequency with the aid of a discriminator that monitors phase deviations between incoming and model signal.

Within regions of multipath ray propagation low signal-to-noise ratios (SNR) are likely to occur causing the discriminator to produce erroneous output values and frequently leading to loss of signal tracking. To solve this problem the Jet Propulsion Laboratory developed and implemented the fly-wheeling tracking technique in the "BlackJack" occultation receivers aboard CHAMP and SAC-C (Satelite de Aplicaciones Cientificas-C) that is activated once SNR falls below a certain threshold. During fly-wheeling the carrier tracking loop is opened and the discriminator values are not extracted from the observed

phase deviations but extrapolated on the basis of phase data samples from the previous few seconds [*Hajj et al.*, 2004].

In open-loop signal tracking mode, finally, the receiver NCO is not driven by the observations, but by an a-priori Doppler frequency model [*Sokolovskiy*, 2001]. The model is derived from a climatology of atmospheric refractivity possibly including meridional, zonal and/or seasonal variations. Small-scale structures of the true Doppler profile, which are caused by multipath signal propagation, are recorded through changes in the residual phase. It is well established that the implementation of open-loop signal tracking in future RO instruments will prevent the receiver from prematurely losing tracking lock and will provide access to carrier phase and amplitude data in the planetary boundary layer (PBL) even at low latitudes [*Sokolovskiy*, 2001; *Sokolovskiy et al.*, 2005].

Motivated by the improvements expected from the open-loop approach we propose a modification of the currently implemented closed-loop tracking that combines the advantages of both techniques. Fig. 1 serves to illustrate our approach. It shows a simulated Doppler profile derived from a tropical radio sonde observation; the sonde data exhibit strong variations in tropospheric humidity. Before about 50 s occultation time, the profile's over-all shape is characterized by the smooth relative motion between the transmitter aboard the occulting GPS and the receiver aboard the LEO spacecraft. Later, the impact of the neutral atmosphere delays the signal reducing the magnitude of the mean phase path acceleration from about 3 $m/s^2$ to less than 1 $m/s^2$. In this simulated event the Doppler frequency visibly deviates at about 50 s occultation time corresponding to a tangent point altitude of about 28 km. We note, however, that RO observations contain information on atmospheric refractivity at significantly higher altitudes reaching the upper stratosphere

[*Kursinski et al.*, 1997]. During the final stage of the occultation, starting at about 67 s occultation time, multipath signal propagation in the mid and lower troposphere produces interference patterns on the smooth background profile. These phase fluctuations are frequently accompanied by amplitude changes of more than an order of magnitude within a few seconds (insert in Fig. 1). The insert shows the Doppler profile within the multipath zone (bottom) together with the corresponding voltage signal-to-noise ratio (top).

Tracking loops of conventional GPS positioning instruments are designed to accommodate arbitrary receiver movements that cause unpredictable phase accelerations; the corresponding voltage signal-to-noise ratio ($SNR_V$) values, however, are in general considered comparatively stable [*Kaplan*, 1996; *Misra and Enge*, 2002]. Occultation receivers, on the other hand, are exposed to strong $SNR_V$ changes with approximately smooth background Doppler frequencies. The results presented here suggest that in radio occultations it is more important to prevent loss-of-lock due to low $SNR_V$ and accept larger NCO phase errors than reducing the NCO phase deviations at the risk of losing the signal within regions of low $SNR_V$.

The outline of the paper is as follows. In section 2 the two observational data sets, a data base of radio sonde observations collected aboard research vessel "POLARSTERN" and archived by Alfred Wegener Institute for Polar and Marine Research (AWI) as well as the CHAMP satellite observations are briefly described. Section 3 discusses the end-to-end simulation chain emphasizing the signal tracking models. In section 4 biases of CHAMP refractivity profiles with respect to meteorological analyses are described and discussed. We restrict the comparisons to atmospheric refractivity, for discussions of temperature and water vapor retrievals see e.g., *Healy* [2001]; *Marquardt et al.* [2001]; *Kursinski and*

*Hajj* [2001]; *Heise et al.* [2005]. Furthermore, the simulation results using closed-loop and open-loop signal tracking schemes are analyzed. Section 5 comments on the feasibility of data wipe-off to permit the implementation of four-quadrant carrier phase extraction and section 6 summarizes the main conclusions.

## 2. Observational data sets

### 2.1. "POLARSTERN" radio sonde data

Starting in December 1982 the AWI radio sonde data set comprises almost 25,000 profiles observed aboard research vessel "POLARSTERN" at latitudes between 78.2°S and 89.9°N. Balloon-borne sondes measure temperature, pressure and humidity data with a vertical resolution of about 20–50 m (corresponding to 5–10 s sampling time at 4–5 m/s balloon rise velocity). Sounding aboard "POLARSTERN" is performed with Vaisala RS80 radio sondes [*Vaisala*, 1989]. The manufacturer quotes the following repeatabilities of calibration: 0.2–0.4°C temperature accuracy between −90°C and +60°C, 0.5 hPa pressure accuracy between 1060 hPa and 3 hPa and 2% RH relative humidity accuracy between 0 and 100% RH. At low temperatures it is known that the accuracy of the humidity measurements decreases further [see e.g., *Leiterer et al.*, 1997].

With very few exceptions critical refraction in the lower troposphere is caused by strong vertical gradients induced by the water vapor field [*von Engeln et al.*, 2003, 2005]; humidity values at high latitudes are in general too low to produce critical refraction layers. Thus, we focus in the following on the subset of 1992 sonde profiles recorded at mid and low latitudes ranging from 45°S to 45°N. The corresponding launch dates cover the time period between 29 December 1982 and 16 June 2005. Figure 2 shows the geographical locations of the corresponding sonde launches.

Refractivity $N$ is calculated from observed pressure $p$, water vapour partial pressure $p_w$ and temperature $T$ from [*Bevis et al.*, 1994]

$$N = k_1 \frac{p - p_w}{T} + k_2 \frac{p_w}{T} + k_3 \frac{p_w}{T^2} \tag{1}$$

with $k_1 = 0.7760$ K/Pa, $k_2 = 0.704$ K/Pa and $k_3 = 3.739 \cdot 10^3$ K$^2$/Pa. Above the balloon burst height $z_B$ the refractivity profiles are extrapolated using

$$N(z) = N(z_B) \exp\left(-\frac{z - z_B}{H}\right) \qquad \text{for} \qquad z > z_B \tag{2}$$

where $H = 7$ km denotes the scale height.

### 2.2. CHAMP satellite observations

As of 30 June 2005 (day of year 181) 320,904 occultation events have been recorded aboard CHAMP since activation of the operational occultation mode on 14 May 2001 (day of year 134). Out of these, 206,422 observations (64.3%) pass the quality criteria imposed by the operational processing system and produce validated refractivity profiles (level-3 data). The current version of the GFZ's occultation processing system (version 5) uses double differencing to retrieve excess phase paths [*Wickert et al.*, 2001, 2004] and the Full Spectrum Inversion (FSI) method [*Jensen et al.*, 2003] to obtain bending angles at tropospheric altitudes. The bending angle profiles are truncated at that impact parameter value where the smoothed FSI amplitude drops to 50% of the maximum value. For a detailed discussion of the data processing and analysis see *Wickert et al.* [2001, 2004].

The observed CHAMP refractivity profiles are intercompared with meteorological analysis results provided by the European Centre for Medium-Range Weather Forecasts (ECMWF). ECMWF pressure and temperature values are calculated by linear interpolation between grid points ($0.5° \times 0.5°$ resolution). Linear interpolation in time is performed

between 6 h ECMWF analyses fields. The vertical resolution of the observed RO refractivity profiles is 200 m [*Wickert et al.*, 2004]; the comparison between observation and ECMWF, however, is performed on the 60 levels provided by the ECMWF atmospheric model ranging from the ground surface up to about 60 km altitude. Geopotential height at each level is calculated from the analysis fields using the hydrostatic equation and converted to geometric height [M. J. Mahoney, A discussion of various measures of altitude, available at http://mtp.jpl.nasa.gov/notes/altitude/altitude.html]. Within the altitude range relevant for this study vertical spacing of the model grid points are of the same order as the observations increasing from about 200 m at 1 km altitude to about 700 m at 10 km altitude. (For a discussion of possible aliasing effects, however, see *Kursinski et al.* [2000]; *Kuo et al.* [2004].)

Negative biases in the lower troposphere are well-known from CHAMP and other satellite RO missions [see e.g., *Rocken et al.*, 1997; *Ao et al.*, 2003; *Hajj et al.*, 2004]. The exact shape of the fractional refractivity error, however, depends on the number of data points retrieved at a given altitude $z$, in the following denoted by $m(z)$; the loss-of-lock altitude $z_{50\%}$ refers to the altitude at which the number of successfully retrieved data points is reduced to 50%. If, e.g., more restrictive quality control criteria are employed removing outlier observations, $z_{50\%}$ increases correspondingly. If the fraction is above 50% within the full altitude range, $z_{50\%}$ is undefined. A plot of $m(z)$ is attached to all figures showing the fractional refractivity error $\Delta N/N_{true} \equiv (N - N_{true})/N_{true}$ in order to emphasize the mutual dependence between fractional refractivity error and $m(z)$.

## 3. End-to-end simulations

Starting from a refractivity profile $N(z)$ the atmospheric propagation of a GPS signal is modelled using the inverse FSI technique [*Gorbunov*, 2003; *Gorbunov and Lauritsen*, 2004]. With the FSI method the simulated amplitude and phase data are converted to bending angle profiles [*Jensen et al.*, 2003]. Finally, refractivity profiles are retrieved by Abel-transforming the bending angle profiles thereby closing the simulation loop [*Ao et al.*, 2003]. Optionally, a simplified signal receiver model can be inserted in the end-to-end simulation chain. Its schematic is shown in Figure 3. For each receiver model and three noise levels 1992 simulation runs are performed using spherically symmetric refractivity fields derived from the "POLARSTERN" radio sonde profiles as described in section 2.1.

For numerical efficiency the simulations are simplified in a number of ways:

1. The GPS and LEO orbits are assumed to be coplanar and circular with radii of $r_G = 26,800$ km and $r_L = 6800$ km, respectively. Thus, FSI and inverse FSI are efficiently implemented using the Fast Fourier Transform without the requirement of vacuum propagation of the wave field or the addition of phase correction terms [*Jensen et al.*, 2003; *Gorbunov*, 2003; *Gorbunov and Lauritsen*, 2004].

2. Since the optical path difference between interfering rays in multipath regions are much smaller than the coarse acquisition code's (C/A code) chip length of 300 m [*Kaplan*, 1996; *Misra and Enge*, 2002], code modulation is not taken into account [*Beyerle et al.*, 2003]. The simulated signal is modulated with the 50 Hz navigation data, though, since the data modulation is relevant for the selected method of carrier phase extraction (see subsection 3.2.1 below).

3. Relativistic Doppler shifts and clock deviations are not included in the simulation. For a detailed discussion see *Ashby* [2003].

4. The carrier tracking loops update only the NCO frequency, phase update loops are not considered [*Stephens and Thomas*, 1995].

5. Since the simulations are focused on altitudes below 10 km, signal propagation through the ionosphere is not taken into account. In real RO events the ionosphere induces carrier phase path deviations on the order of several tens of meters which have to be corrected for by simultaneous observations at both GPS frequencies, L1 and L2 [see e.g., *Syndergaard*, 2000]. In this study, however, dispersion is ignored and only L1 data is generated.

### 3.1. Forward propagation

The optical path length differences between interfering rays in multipath regions are much smaller than the C/A code chip (and navigation bit) lengths, as already indicated [*Beyerle et al.*, 2003]. In order to efficiently simulate the propagation process from the transmitter to the receiver the signal is modelled as modulation-free, i.e. a pure tone. Atmospheric propagation of GPS signals is implemented using the inverse FSI technique [*Gorbunov*, 2003; *Gorbunov and Lauritsen*, 2004]. First, the bending angle profile $\alpha(p)$ as a function of impact parameter $p$ is determined from the observed refractive index profile $n(p)$ using the inverse Abel transform [*Fjeldbo et al.*, 1971]

$$\alpha(p) = -2\,p \int_{p}^{\infty} \frac{dx}{\sqrt{x^2 - p^2}} \frac{d\ln(n(x))}{dx} \tag{3}$$

where the integral's upper limit is approximated as $r_E + 150$ km. From $\alpha(p)$ the signal amplitude $A(t)$ and phase $\Phi(t)$ at the LEO's location is calculated with the inverse FSI

method [*Gorbunov*, 2003; *Gorbunov and Lauritsen*, 2004]. Random sign changes every 20 ms simulate the 50 Hz data modulation of the signal $u(t)$, i.e.

$$u(t) \equiv D(t)\, A(t)\, \cos(\Phi(t) - \Phi_0) \tag{4}$$

with data modulation $D(t) = \pm 1$ [*Ao et al.*, 2003] and $\Phi_0 \equiv \Phi(t = 0)$. $D(t)$ is taken to be piecewise constant over periods of 20 ms.

### 3.2. Receiver models

The receiver tracks the signal $u(t)$ by correlating $u(t)$ with replica signals $v^i(t) \equiv \cos[\Phi^{NCO}(t)]$ and $v^q(t) \equiv -\sin[\Phi^{NCO}(t)]$. The replicas $v^i(t)$ and $v^q(t)$ are generated by the receiver's NCO [*Kaplan*, 1996; *Tsui*, 2000; *Misra and Enge*, 2002]. In our simulation the NCO's frequency $f^{NCO}(t)$ is updated at a rate of $1/T = 1$ kHz, i.e. $f^{NCO}(t)$ is piecewise constant for $t_n \le t < t_n + T$, $f_n^{NCO} \equiv f^{NCO}(t_n)$. Provided the amplitude $A(t)$ and frequency $f(t) \equiv 1/(2\pi)\, d\Phi/dt$ can be approximated as piecewise constant functions, $A_n \equiv A(t_n)$ and $f_n \equiv f(t_n)$, the inphase and quadphase correlation sums are given by

$$\begin{aligned} i_n &\equiv \frac{2}{T} \int_{t_n}^{t_n+T} u(t)\, v^i(t)\, dt + N_n^i \\ &\approx D_n\, A_n\, \mathrm{sinc}(\pi\, \Delta f_n\, T)\, \cos(\pi\, \Delta f_n\, T + \Delta\Phi_n) + N_n^i \\ &= D_n\, A_n\, \mathrm{sinc}(\pi\, \Delta f_n\, T)\, \cos\Big(\frac{\Delta\Phi_n + \Delta\Phi_{n+1}}{2}\Big) + N_n^i \end{aligned} \tag{5}$$

and

$$\begin{aligned} q_n &\equiv \frac{2}{T} \int_{t_n}^{t_n+T} u(t)\, v^q(t)\, dt + N_n^q \\ &\approx D_n\, A_n\, \mathrm{sinc}(\pi\, \Delta f_n\, T)\, \sin(\pi\, \Delta f_n\, T + \Delta\Phi_n) + N_n^q \\ &= D_n\, A_n\, \mathrm{sinc}(\pi\, \Delta f_n\, T)\, \sin\Big(\frac{\Delta\Phi_n + \Delta\Phi_{n+1}}{2}\Big) + N_n^q \end{aligned} \tag{6}$$

respectively, with $\mathrm{sinc}(x) \equiv \sin(x)/x$ and $D_n \equiv D(t_n)$. Here, $\Delta f_n \equiv f_n - f_n^{NCO}$ and $\Delta\Phi_n \equiv \Phi_n - \Phi_n^{NCO}$ denote the difference between the true frequency $f_n$ and the NCO frequency $f_n^{NCO}$ and the difference between the true phase $\Phi_n$ and the NCO phase $\Phi_n^{NCO}$, respectively. Here and in the following the subscript $n$ denotes the corresponding function value at time $t_n$, i.e. $f_n \equiv f(t_n)$ and $\Phi_n \equiv \Phi(t_n)$, except where noted otherwise. The NCO and true phases follow from

$$\begin{aligned} \Phi_n^{NCO} &\equiv 2\pi\, T \sum_{j=1}^{n-1} f_j^{NCO} \\ \Phi_n &\equiv 2\pi\, T \sum_{j=1}^{n-1} f_j \ . \end{aligned} \tag{7}$$

We note that $\Phi_n^{NCO}$ and $\Phi_n$ are accumulated phases and not restricted to the interval $[-\pi, +\pi]$. Gaussian white noise, $N_n^i$ and $N_n^q$, with zero mean and standard deviations

$$\sigma(N_n^{i,q}) = \frac{A^{(0)}}{\sqrt{2\,T\,10^{C/N_0/10}}} \tag{8}$$

is added to the correlation sums, $i_n$ and $q_n$ (Eqns. 5 and 6), where $A^{(0)}$ denotes the amplitude for vacuum propagation and $C/N_0$ is the carrier-to-noise density ratio expressed in dB Hz [*Kaplan*, 1996].

The total accumulated phase is the sum of NCO phase $\Phi_n^{NCO}$ and residual phase $\Phi_n^R$ (see section 3.2.1)

$$\varphi_n^{Rcv} \equiv \Phi_n^{NCO} + \Phi_n^R \ . \tag{9}$$

Finally, output data volume is compressed from $1/T = 1$ kHz to 50 Hz by coherent summation over $K = 20$ samples

$$\begin{aligned} I_k &= \sum_{j=K\cdot(k-1)+1}^{K\cdot k} i_j \\ Q_k &= \sum_{j=K\cdot(k-1)+1}^{K\cdot k} q_j \end{aligned} \tag{10}$$

$$\Phi_k^{Rcv} = \frac{1}{K} \sum_{j=K\cdot(k-1)+1}^{K\cdot k} \varphi_j^{Rcv} .$$

In the following, $I_k$ and $Q_k$ are denoted as coherent inphase and quadphase correlation sums, respectively. We note that according to Eqn. 10 $\Phi_k^{Rcv}$ is taken to be the mean value of $\varphi_j^{Rcv}$, *Thomas* [1989] discusses more sophisticated alternatives. From the coherent correlation sums the signal amplitudes

$$A_k^{Rcv} = \sqrt{(I_k)^2 + (Q_k)^2} \tag{11}$$

are obtained. Signal tracking is accomplished in either closed-loop or open-loop mode. The two modes will be discussed in section 3.2.2 and 3.2.3.

### 3.2.1. Residual phase extraction

The residual phases $\Phi_n^R$ (Eqn. 9) are extracted from the correlation sums (Eqns. 5 and 6) using two different methods. Within the two-quadrant phase extraction scheme the residual phases are

$$\Phi_{n+1}^R = \mathrm{atan}\left(\frac{q_n}{i_n}\right) . \tag{12}$$

Provided $|i_n| \gg |N_n^i|$ and $|q_n| \gg |N_n^q|$ (Eqns. 5 and 6) Eqn. 12 may be approximated by

$$\Phi_{n+1}^R \approx \mathrm{atan}\left(\tan\left(\frac{\Delta\Phi_n + \Delta\Phi_{n+1}}{2}\right)\right) . \tag{13}$$

Two-quadrant phase extraction is commonly used in GPS receivers since $\Phi_{n+1}^R$, as derived from Eqn. 13, does not dependent on the data modulation values $D_n$ [*Kaplan*, 1996]. On the other hand, the validity of Eqns. 12 (and 13) is restricted to the phase interval $[-\pi/2, +\pi/2]$. If the phase deviations exceed $\pm\pi/2$ an erroneous offset of $\pm\pi$ between derived residual phase and true phase error is introduced since $\mathrm{atan}(\tan(x)) = x$ only if $-\pi/2 \leq x \leq \pi/2$, but $\mathrm{atan}(\tan(x)) = x \pm \pi$ otherwise.

To obtain valid residual phases for phase deviations larger than $+\pi/2$ and smaller than $-\pi/2$ the following four-quadrant phase extraction scheme is used

$$\Phi^R_{n+1} = \mathrm{atan2}\Big(\frac{q_n}{D_n}, \frac{i_n}{D_n}\Big) \ . \tag{14}$$

Four-quadrant phase extraction according to Eqn. 14, though, presupposes knowledge of the data modulation $D_n$.

In closed-loop mode the phase-locked loop (PLL) steers the residual phase $\Phi^R_{n+1}$ towards zero, i.e. $|i_n| \gg |q_n|$ if the tracking loop is locked to the signal. In open-loop mode (section 3.2.3), however, received and replica signals are no longer phase-locked, $\Phi^R_{n+1}$ possibly exceeds the interval $[-\pi, +\pi]$ and use of Eqn. 14 would introduce a cycle slip whenever $\Phi^R_{n+1}$ passes $\pm\pi$. These cycle slips are eliminated by adding the number of full cycles to $\Phi^R_{n+1}$, i.e. Eqn. 14 is modified by

$$\Phi^R_{n+1} = \mathrm{atan2}\Big(\frac{q_n}{D_n}, \frac{i_n}{D_n}\Big) + C_n \tag{15}$$

where

$$C_n = \begin{cases} C_{n-1} - 2\pi & : \ \mathrm{atan2}\Big(\frac{q_n}{D_n}, \frac{i_n}{D_n}\Big) - \mathrm{atan2}\Big(\frac{q_{n-1}}{D_{n-1}}, \frac{i_{n-1}}{D_{n-1}}\Big) < -\pi \\ C_{n-1} + 2\pi & : \ \mathrm{atan2}\Big(\frac{q_n}{D_n}, \frac{i_n}{D_n}\Big) - \mathrm{atan2}\Big(\frac{q_{n-1}}{D_{n-1}}, \frac{i_{n-1}}{D_{n-1}}\Big) > +\pi \\ C_{n-1} & : \ \mathrm{else} \end{cases} \tag{16}$$

and $C_1 = 0$.

In the current CHAMP occultation receiver closed-loop tracking with two-quadrant phase extraction is implemented [*Ao et al.*, 2003]. Four-quadrant phase extraction, on the other hand, records the data modulation bits and introduces half-cycles whenever a bit transition occurs. Thus, four-quadrant phase extraction presupposes the removal of the 50 Hz data modulation prior to signal correlation (data demodulation or data wipe-off)

and necessitates knowledge of the navigation message. We comment on the feasibility of data wipe-off in section 5.

### 3.2.2. Closed-loop tracking

To study the sensitivity of retrieved refractivities with respect to the chosen tracking loop parameters, the simulation receiver's carrier loop bandwidths are varied between 5 and 30 Hz and loops of order two and three are implemented. In closed-loop mode the NCO frequency is adjusted every C/A code period (about 1 ms) by $\delta f_{n+1}^{NCO} \equiv f_{n+1}^{NCO} - f_n^{NCO}$. The frequency adjustment for the time interval $[t_{n+1}, t_{n+2}]$ is

$$\delta f_{n+1}^{NCO} = \frac{1}{T}\left(\frac{K_1^{(2)} + K_2^{(2)}}{2\pi}\,\Phi_{n+1}^R + \frac{-K_1^{(2)}}{2\pi}\,\Phi_n^R\right) \tag{17}$$

(second order loop) or

$$\delta f_{n+1}^{NCO} = \delta f_n^{NCO} + \frac{1}{T}\left(\frac{K_1^{(3)} + K_2^{(3)} + K_3^{(3)}}{2\pi}\,\Phi_{n+1}^R + \frac{-2\,K_1^{(3)} - K_2^{(3)}}{2\pi}\,\Phi_n^R + \frac{K_1^{(3)}}{2\pi}\,\Phi_{n-1}^R\right) \tag{18}$$

(third order loop), respectively, where the residual phase $\Phi_n^R$ is given in radian and $K_1^{(2)} = 7.358 \cdot 10^{-2}$, $K_2^{(2)} = 2.810 \cdot 10^{-3}$ for a standard-underdamped second order loop and $K_1^{(3)} = 7.172 \cdot 10^{-2}$, $K_2^{(3)} = 2.383 \cdot 10^{-3}$, $K_3^{(3)} = 3.020 \cdot 10^{-5}$ for a standard-underdamped third order loop [*Stephens and Thomas*, 1995]. In both cases tracking loop bandwith is taken to be 30 Hz. For comparison simulation runs with loop bandwidth reduced to 5 Hz are performed as well. 5 Hz was chosen since it is the smallest bandwidth value given by *Stephens and Thomas* [1995]. The corresponding third order loop parameters are $K_1^{(3)} = 1.283 \cdot 10^{-2}$, $K_2^{(3)} = 7.365 \cdot 10^{-5}$ and $K_3^{(3)} = 1.590 \cdot 10^{-7}$. With $\delta f_{n+1}^{NCO}$ the NCO frequency of the $(n+1)$th update interval follows from $f_{n+1}^{NCO} = \delta f_{n+1}^{NCO} + f_n^{NCO}$ and subsequently $i_{n+1}$ and $q_{n+1}$ are calculated using Eqns. 7, 5 and 6.

### 3.2.3. Open-loop tracking

Open-loop tracking is commonly considered a possible solution to the problem of premature loss-of-lock in closed-loop receivers [*Sokolovskiy*, 2001]. In open-loop mode the loop feedback $\delta f_{n+1}^{NCO}$ is calculated from a Doppler frequency model $f^{model}(t_n) \equiv f_n^{model}$, i.e.

$$f_{n+1}^{NCO} = f_{n+1}^{model} \tag{19}$$

and therefore

$$\delta f_{n+1}^{NCO} = f_{n+1}^{model} - f_n^{NCO} \, . \tag{20}$$

For simplicity, in this study the model $f_n^{model}$ is taken to be ensemble average

$$f_n^{model} \equiv \frac{1}{N_R} \sum_{j=1}^{N_R} f_n^{(j)} \equiv \langle f_n^{(j)} \rangle \tag{21}$$

where $N_R = 1992$ and $f_n^{(j)}$ is the true signal frequency derived from the $j$th simulated Doppler profile at time interval $n$. The one-sigma standard deviation is about 10–20 Hz in good agreement with *Sokolovskiy* [2001]. Total phase is calculated from Eqn. 9, with $\Phi_n^R$ extracted from Eqn. 15 and $\Phi_n^{NCO}$ is derived from the NCO frequency (Eqn. 7). Analogous to the closed-loop case the sampling rate is reduced from 1 kHz to 50 Hz using Eqn. 10 and Eqn. 11 yields the signal amplitude. Thus, in open-loop mode the total phase is not a raw data product provided by the receiver, but instead is calculated in post-processing from the inphase and quadphase correlation sums taking into account the (known) 50 Hz navigation data.

### 3.2.4. Fly-wheel mode tracking

The first occultation measurements from the proof-of-concept GPS/MET mission frequently suffered from loss-of-lock already in the upper or mid troposphere in particular at low latitudes [*Rocken et al.*, 1997]. To solve this problem Jet Propulsion Laboratory

developed and implemented the fly-wheeling tracking method [*Hajj et al.*, 2004]. Fly-wheeling mode was successfully used in later phases of the GPS/MET mission and is the nominal tracking mode on the CHAMP and SAC-C satellites.

Fly-wheel tracking is activated when $\mathrm{SNR_V}$ drops below a predefined threshold value $\mathrm{SNR_V^\star}$. Once activated, the tracking loop is opened and $f_{n+1}^{NCO}$ is calculated from the previous $L$ NCO frequencies by extrapolating a polynomial fit through $f_{n-L+1}^{NCO}, \ldots, f_n^{NCO}$. Thus, during fly-wheeling the carrier tracking loop is no longer phase-locked to the signal $u(t)$. The phasor $I + i\,Q$ starts to rotate freely in $I - Q$ space, effectively randomizing the residual phase values and thereby enhancing the occurrence probability of carrier phase cycle slips. However, signal loss is less likely during fly-wheeling since large residual phase errors no longer cause $f_n^{NCO}$ to sheer out.

Our fly-wheeling simulations show that the results depend strongly on the selected fly-wheeling parameters: the number of samples $L$ included in the polynomial fit, the degree of the extrapolation polynomial, the amplitude thresholds for activation and deactivation, possible time delays, etc. In our implementation the following parameters were found to give best results: $L = 2000$ corresponding to a time period of 2 s, a linear fit and a threshold value of $\mathrm{SNR_V^\star} = 40$ V/V. If the observed amplitude falls below $\mathrm{SNR_V^\star}$ for more than 100 ms, fly-wheeling is activated for at least 2 s. We stress that the design choices of our fly-wheeling implementation were made to achieve consistency with the CHAMP occultation data; the implementation should not be regarded as an accurate model of the "BlackJack" receiver aboard CHAMP.

### 3.3. Backward model

From the amplitudes $A_k^{Rcv}$ and phases $\Phi_k^{Rcv}$ (Eqn. 10) bending angle profiles are derived with the FSI technique [*Jensen et al.*, 2003; *Gorbunov and Lauritsen*, 2004]. The bending angle profiles are inverted to refractivity profiles using the Abel transform [*Fjeldbo et al.*, 1971] thereby closing the simulation chain.

## 4. Analysis and discussion

### 4.1. Sonde and satellite observations

From the "POLARSTERN" in-situ measurements all soundings located between 45°S and 45°N latitude are selected and the refractivity profiles $N(z)$ are calculated. 84 out of 2076 soundings are removed from the data set since they contain discontinuities in the relative humidity values exceeding 50% RH or consist of less than 10 measurement samples. The remaining 1992 profiles are linearly interpolated on an altitude grid with 5 m resolution and low-pass filtered using a running mean with 150 m width to reduce measurement noise introduced by the humidity sensor [*Vaisala*, 1989]. We ignore the sonde's horizontal motion during ascent (or, equivalently, we assume spherical symmetry of the refractivity field) and identify the changes of $N(z)$ with the vertical refractivity gradient $dN/dz$. The occurrence distribution of the smallest value of $dN/dz$ is shown in Fig. 4. 58.3% (1162 profiles) exhibit critical refraction with $dN/dz < -157\ \mathrm{km}^{-1}$ (dashed line). These percentage estimates, however, should be regarded as an upper limit for the occurrence of critical refraction in the marine environment at low and mid latitudes, since radio sonde data represent point measurements without information on the horizontal extent of the observed layers [see e.g., *von Engeln et al.*, 2003]. The probability for the occurrence of critical refraction as a function of altitude can be inferred from Fig. 5

which shows the altitude distribution of the highest layer obeying $dN/dz < -157$ km$^{-1}$. Fig. 5 suggests that critical refraction is a phenomenon restricted to the PBL at altitudes below 2–2.5 km. Above 3 km critical layers are unlikely to occur [see also *Gorbunov et al.*, 1996].

The CHAMP refractivity bias derived from 11,626 observations over the Atlantic ocean between 45°S–0°S, 45°W–15°E and 0°N–45°N, 45°W–15°W is plotted in Fig. 6 (solid lines). Whilst the $N$-bias is below 0.2% in the mid troposphere at altitude between 5 and 13 km, it decreases to −3% within the PBL. The occurrence distribution shown in Fig. 5 suggests that critical refraction contributes to the observed deviation only below 3 km. The smaller negative bias between 3 and 5 km altitude, however, most likely is caused by the receiver tracking as discussed in section 4.2.

The large volume of the CHAMP occultation data set allows for a $N$-bias analysis not only in terms of zonal and/or meridional averages but also as a function of longitude and latitude. 206,422 profiles of the fractional refractivity deviation between CHAMP and ECMWF are sorted in $10° \times 10°$ longitude/latitude bins. Within each bin the mean value between 3 and 5 km altitude is computed and plotted in Fig. 7. On average, there are $306 \pm 101$ observations per bin.

At high latitudes the fractional refractivity error remains below ±0.3%, at mid and low latitudes the bias reaches below −1% on a global scale. The geographical distribution, however, exhibits pronounced patterns with small and medium-scale biases exceeding +1% over South America and −2% over the eastern tropical Pacific. The simulation results discussed below suggest that the negative bias is consistently explained by receiver-induced tracking errors (within the altitude range of 3–5 km the occurrence of critical refraction

is not expected). The explanation for the positive biases over the Amazon region and Indonesia requires a detailed analysis which is beyond the scope of this study. One of the possibilities that should be investigated is the occurrence of positive vertical refractivity gradients (refractivity increases with altitude) leading to subrefraction; *Sokolovskiy* [2004] discusses an individual sonde profile that exhibits subrefraction and yields a positive refractivity bias. The solid white lines mark the geographical region of observations plotted as solid lines in Fig. 6, the Amazon data is plotted as dashed lines. Fig. 6 demonstrates the positive bias of this subset and its enhanced standard deviation (thin dashed lines). The corresponding 50%-altitudes are 2.5 km (Atlantic) and 2.8 km (Amazon region), respectively.

### 4.2. End-to-end simulations

The task of interpreting the $N$-bias below 5 km (Fig. 6) is approached by a series of end-to-end simulation runs; the results are presented in Figs. 8–13. The plots show the mean fractional difference between retrieved and true refractivity in the left panel (thick lines). Thin lines mark the one-sigma standard deviation. In addition, the number of retrieved data points as function of altitude is indicated as well (right panel).

The simulations are performed for signal-to-noise density ratios of 40, 45 and 50 dB Hz. This choice is motivated by $\mathrm{SNR_V}$ values typically observed in CHAMP occultation events. Fig. 14 shows the normalized histogram distribution of C/A $\mathrm{SNR_V}$ derived from 4526 CHAMP observations collected during January 2004. Whilst at mid and high latitudes $\mathrm{SNR_V}$ varies between about 200 and 900 V/V with a mean value of 576 V/V (dashed line), in the Tropics $\mathrm{SNR_V}$ extends from about 200 V/V ($\mathrm{C/N_0}$ = 43.0 dB Hz) to about 700 V/V ($\mathrm{C/N_0}$ = 53.9 dB Hz) with a mean value of 511 V/V (solid).

The simulation results without signal tracking (ideal receiver) are plotted in Fig. 8. In a control run we restrict the comparison to the height range above $z_{CR} + 100$ m and obtain a mean fractional retrieval error and standard deviation below 0.01% and 0.03%, respectively (dashed lines). Here, $z_{CR}$ denotes the largest altitude where critical refraction is observed. As noted above, 58.3% of the refractivity profiles exhibit critical refraction; below 3 km this subset generates a negative bias of up to $-1$% and a standard deviation of about 2% (solid lines).

All in all, the simulations are performed with five different signal tracking models:

1. Model A is the ideal receiver which exactly reproduces the signal at its input; noise contributions are not included in the simulations using model A.

2. The reference receiver (model B) uses closed-loop tracking, two-quadrant phase extraction with a third order loop and 30 Hz loop bandwidth; model B is capable of fly-wheeling. Qualitatively, model B corresponds to the current configuration of the "Black-Jack" receiver aboard CHAMP.

3. Model C is the implementation of an open-loop receiver which outputs inphase and quadphase correlation sums together with the phase model. In post-processing the total carrier phase $\varphi_n^{Rcv}$ (Eqn. 9) is extracted from the correlation sums taking into account the 50 Hz navigation bits (subsection 3.2.3).

4. Model D uses closed-loop tracking with a third order loop, however, at reduced loop bandwidth of 5 Hz; fly-wheeling is deactivated.

5. Model E is an implementation of closed-loop tracking with 30 Hz loop bandwidth, but the loop order is reduced from three to two. Model E as well as model D employ four-quadrant phase extraction (data wipe-off), again fly-wheeling is not active.

The models' receiver parameters are summarized in Table 1.

The retrieval results obtained from models B–E are presented in Figs. 9–13. The left panel of each figure shows mean and one-sigma standard deviation profiles obtained by linear interpolation of the individual retrieval results on a equidistant altitude grid with 50 m step size; the vertical resolution of the individual profiles is about 10–15 m. No profile selection with respect to critical refraction has been performed.

The retrieval results may directly be compared to the solid line in Fig. 8, left panel. For that purpose the ideal receiver profile (thick solid line in Fig. 8, left panel) is repeated in Figs. 9–13. We note that $m(z)$ in Fig. 8, right panel, starts to decrease already at 2 km altitude. Below that altitude the occurrence of critical layers introduces sharp cut-outs in the FSI amplitude. If these amplitude drops reach below 50% of the maximum FSI amplitude the bending angle profile is clipped already at that altitude (see section 2.2). By adding noise to the signal (receiver models B–E) the FSI amplitude gaps are washed out and drops below 50% occur less frequently. Within the PBL, therefore, $m(z)$ (shown in Figs. 9–13, left panels) may exceed the number data points obtained from the ideal receiver (Fig. 8).

The onset of a decrease in $m(z)$ already at 4–8 km altitude (Fig. 9, right panel) shows that the fly-wheeling receiver (Model B) frequently loses tracking lock in the mid troposphere before reaching layers of critical refraction. Since loss-of-lock tends to occur at or above critical layers one would expect that the subset of successfully tracked signals minimizes the bias. However, a significant negative bias is observed below 5 km altitude. Within the PBL critical refraction might contribute to the negative $N$-bias; above 3 km

receiver-induced errors are the most likely cause, since the occurrence of critical refraction above that altitude can be excluded.

The comparison between simulation results obtained by the open-loop receiver (Fig. 10) and results produced by the fly-wheeling receiver with two-quadrant phase extraction (Fig. 9) highlights the significant negative bias and enhanced standard deviation introduced by the latter. The open-loop refractivities (dashed, dashed-dotted and dotted lines in Fig. 10) exhibit almost no bias and reduced standard deviation with respect to the ideal receiver (solid line).

The choice of the open-loop Doppler model (Eqn. 21) implies that the retrieved frequency profiles $f_n^{Rcv}$ are bias-free with respect to the true profiles. In order to address the question whether $f_n^{Rcv}$ remains bias-free if the model is biased with respect to the truth, i.e. $\langle f_n^{model} - f_n^{(j)} \rangle \neq 0$, the open-loop simulation was repeated with the Doppler model $f_n^{model}$ replaced by $f_n^{model} + \Delta f$ and $\Delta f = +10$ Hz; Fig. 11 shows the result. Whereas the frequency offset has no visible effect at density ratios of 45 and 50 dB Hz, at $C/N_0 = 40$ dB Hz a positive bias on the order of 0.5% is observed. Clearly, these systematic deviations between retrieved and true frequencies are correlated with low signal strength. The relation between frequency bias and $\mathrm{SNR_V}$ is shown in Fig. 15 using data from simulation run #10 (cf. Fig 1). The mean deviation averaged over $\mathrm{SNR_V}$ bins of width 10 V/V is plotted for $\Delta f = 0$ Hz (solid line), $\Delta f = +10$ Hz (dashed) and $\Delta f = -10$ Hz (dashed-dotted). For clarity the scale of vertical axis has been restricted to $\pm 5$ Hz, the individual data points (marked in grey) extend to about $\pm 40$ Hz at $\mathrm{SNR_V} < 20$ V/V.

The fact that a bias in the model frequency $f_n^{model}$ introduces a corresponding bias in the retrieved frequency $f_n^{Rcv}$ for $\mathrm{SNR_V} \to 0$ can be understood by writing Eqn. 9 in terms

of frequencies; we obtain

$$f_n^{Rcv} \;=\; f_n^{model} + (\Phi_{n+1}^R - \Phi_n^R)/(2\pi\, T)\;. \tag{22}$$

with $f_n^{model} = f_n^{NCO}$. For $\mathrm{SNR_V} \to 0$ the residual phases $\Phi_n^R$ and $\Phi_{n+1}^R$ are randomly distributed between $-\pi$ and $+\pi$,

$$\langle f_n^{Rcv} \rangle = f_n^{model} + \langle \Phi_{n+1}^R - \Phi_n^R \rangle/(2\pi\, T) \to f_n^{model}\;. \tag{23}$$

Here, $\langle\cdot\rangle$ denotes the ensemble mean over the simulation data set (Eqn. 21). If $f_n^{model}$ is biased with respect to the true frequency, then, in the limit $\mathrm{SNR_V} \to 0$, $f_n^{Rcv}$ will be biased as well. We note, however, that this open-loop bias is a minor effect in the mid and lower troposphere and is relevant only for weak signals (Fig. 11).

In comparing the results obtained by open- and closed-loop tracking it is instructive to illuminate the role played by the NCO phase. In the closed-loop approach the loop is designed to follow all phase accelerations within multipath regions; the residual phase adds only minor corrections to the total phase. In open-loop mode, on the other hand, the NCO phase characterizes the smooth background state and the small-scale structures induced by multipath interference patterns are captured by the residual phase. We propose a combination of both techniques: the sensitivity of the loop is degraded to achieve a better resistivity against noise-induced phase accelerations. The multipath interference patterns are then recovered to a lesser extent from the NCO phase and to a higher degree from the residual phase (see discussion of Fig. 16 below).

Two methods to reduce the loop sensitivity are investigated: first, the loop bandwidth is reduced from 30 to 5 Hz (model D), the result is plotted in Fig. 12. The comparison with Fig. 9 shows an improvement, both in terms of bias and standard deviation. In

addition, receiver model D tracks to significantly lower altitudes with $z_{50\%}$ of 0.11, 0.025 and 0.039 km for $C/N_0$ = 40, 45 and 50 dB Hz, respectively. Still, at $C/N_0$ =40 dB Hz the retrieved refractivities are biased by up to +0.5% and standard deviations exceed 2%.

In the second approach the loop order is reduced from three to two, whereas the loop bandwidth is kept at 30 Hz. The retrieval results plotted in Fig. 13 compare favorably with the open-loop results (Fig. 10) with respect to bias, standard deviation and loss-of-lock altitude. Indeed, closed-loop tracking with a second order loop seems to be less sensitive to noise-induced phase accelerations and succeeds in shifting the loss-of-lock altitude downwards. The improvements gained by model E over a third order loop, but otherwise identical receiver is exemplarily illustrated in Fig. 16. It shows the NCO frequency profiles obtained from simulation run #10 (cf. Fig. 1) during the last 10 s of the occultation event. The second order loop (model E) maintains lock until 90.5 s occultation time, whereas the third order loop loses the signal already 5 s earlier. For comparison the true frequency (thin solid line) is plotted as well. Comparison with the insert in Fig. 1 shows that the third order loop's loss-of-lock at 85.2 s is not triggered by enhanced phase accelerations, but by low $SNR_V$. We note that in this simulation event the fly-wheeling receiver (model B) ceases to track the signal already at 67.5 s occultation time.

## 5. Feasibility of data wipe-off

It was noted that signal tracking using four-quadrant phase extraction requires knowledge of the 50 Hz data bit in order to demodulate the signal. Since to the best of our knowledge the GPS navigation messages are not publicly available prior to transmission the data bits have to be predicted, transmitted by the receiver and compared to the true

data bits (monitored by an appropriate ground station network) during post-processing. We briefly discuss the feasibility of this approach.

The GPS navigation message is organized in frames of 1500 bit transmitted during 30 s. Each frame consists of five 300 bit subframes [*Kaplan*, 1996; *Misra and Enge*, 2002]. Subframes 1 to 3 repeat every 30 s, subframes 4 and 5 change 25 times increasing the repetition interval to 12.5 min. Demodulation is performed with predicted navigation data bits $D_n^{(p)}$. A receiver capable of data wipe-off outputs $D_n^{(p)}$ in addition to phase and amplitude data. During post-processing of the data $D_n^{(p)}$ is compared to the true data bits $D_n$ and those occultation events recorded with a wrong prediction are flagged and removed from data set.

In order to obtain an estimate on the predictability of $D_n$, one week of GPS data collected by a modified GPS receiver at GeoForschungsZentrum Potsdam (52.38°N, 13.07°E) was analyzed. From 13 June to 19 June 2004 (GPS week number 1275) the instrument recorded the navigation messages of all 28 active GPS satellites, in total 676,873 subframes. Our prediction algorithm assumes that the 53 different types of subframes (subframes 1–3 and 25 versions of subframe 4 and 5) remain constant with a repeat cycle of 12.5 min except for the time information (time-of-week count message) [*Kaplan*, 1996; *Misra and Enge*, 2002]. The predicted time tag in the second word of each subframe is obtained by incrementing the time-of-week count message. Despite the algorithmic simplicity 664,717 subframes are predicted correctly, only 12,156 out of 676,873 (less than 2%) predictions fail.

## 6. Conclusions

An analysis of 1992 radio sonde soundings over the Atlantic ocean between 45°S and 45°N shows that critical refraction in the marine environment is restricted to altitudes below 3 km. Within the PBL more than 50% of the observations show vertical refractivity gradients below the value of $-157$ km$^{-1}$.

CHAMP refractivities observed within the same geographical region exhibit a negative bias with respect to ECMWF at altitudes of up to 5 km. The bias below 3 km may contain contributions from critical refraction; in most occultation events, however, the fly-wheeling receiver loses lock at or above the critical refraction layer. The qualitative agreement between the simulated and observed results suggests that the CHAMP bias above 3 km is related to fly-wheeling and two-quadrant phase extraction. Receivers using open-loop tracking or closed-loop tracking with a reduced loop order yield improvements in the mid and lower troposphere at altitude below 6–8 km in terms of retrieval bias, standard deviation and loss-of-lock altitude. At low signal-to-noise ratios of 141 V/V ($C/N_0$ = 40 dB Hz) our open-loop tracking results are biased towards the Doppler frequency model. Though, this bias should not be regarded as a serious limitation of future open-loop receivers, since their specifications call for significantly larger $C/N_0$ values.

The simulation results show that open-loop tracking as well as closed-loop tracking with reduced loop order yield significantly smaller biases and standard deviations of the fractional refractivity errors compared to fly-wheeling enabled receivers. Thus, we consider second order closed-loop tracking a viable alternative to open-loop. Regardless of which option is selected in future receivers we expect the most significant bias reduction in the mid troposphere at altitudes between 3 and 5 km. Below 3 km a large fraction of the observations at low latitudes are affected by critical refraction layers causing current

RO receivers to lose tracking lock too early. Since the occurrence of critical refraction introduces negative biases as well, provided signal tracking lock is maintained down to the ground, the expected bias reduction due to improved tracking techniques may partly be outweighed by the lowering of the loss-of-lock altitude. Furthermore, throughout the lower and mid troposphere the standard deviation of the fractional refractivity error is estimated to be significantly smaller compared to current CHAMP observations.

**Acknowledgments.** We thank H.-H. Benzon, J. Christensen, A. von Engeln, M. E. Gorbunov, A. S. Jensen, T. Meehan, R. Neuber and S. Sokolovskiy for helpful suggestions and fruitful discussions. Comments by anonymous reviewers on several versions of this paper are gratefully acknowledged. Their corrections, suggestions and remarks considerably improved the quality of this study. The European Centre for Medium-Range Weather Forecasts provided meteorological analysis fields. Part of this work was performed when the first author was GRAS SAF visiting scientist at the Danish Meteorological Institute, Copenhagen, Denmark.

## References

Ao, C. O., T. K. Meehan, G. A. Hajj, A. J. Mannucci, and G. Beyerle (2003), Lower-troposphere refractivity bias in GPS occultation retrievals, *J. Geophys. Res.*, *108*(D18), 4577, doi:10.1029/2002JD003216.

Ashby, N. (2003), Relativity in the Global Positioning System, *Living Rev. Relativity*, *6*(1), [Online article]: cited on 26 Jul 2005, http://www.livingreviews.org/lrr-2003-1.

Bevis, M., S. Businger, S. Chiswell, T. A. Herring, R. A. Anthes, C. Rocken, and R. H. Ware (1994), GPS meteorology: Mapping zenith wet delays onto precipitable water,

*Journal of Applied Meteorology*, *33*(3), 379–386.

Beyerle, G., M. E. Gorbunov, and C. O. Ao (2003), Simulation studies of GPS radio occultation measurements, *Radio Sci.*, *38*(5), 1084, doi:10.1029/2002RS002800.

Fjeldbo, G., A. J. Kliore, and V. R. Eshleman (1971), The neutral atmosphere of Venus as studied with the Mariner V radio occultation experiments, *Astron. J.*, *76*(2), 123–140.

Gorbunov, M. E. (2002), Radio-holographic analysis of Microlab-1 radio occultation data in the lower troposphere, *J. Geophys. Res.*, *107*(D12), 4156, doi:10.1029/2001JD000889.

Gorbunov, M. E. (2003), An asymptotic method of modeling radio occultations, *J. Atmos. Solar-Terr. Phys.*, *65*, 1361–1367, doi:10.1016/j.jastp.2003.09.001.

Gorbunov, M. E., and K. B. Lauritsen (2004), Analysis of wave fields by Fourier integral operators and their application for radio occultations, *Radio Sci.*, *39*, RS4010, doi: 10.1029/2003RS002971.

Gorbunov, M. E., S. V. Sokolovsky, and L. Bengtsson (1996), Space refractivity tomography of the atmosphere: Modeling of direct and inverse problems, *Report 210*, Max-Planck-Institut für Meteorologie, Germany, Hamburg.

Hajj, G. A., E. R. Kursinski, L. J. Romans, W. I. Bertiger, and S. S. Leroy (2002), A technical description of atmospheric sounding by GPS occultation, *J. Atmos. Solar-Terr. Phys.*, *64*(4), 451–469.

Hajj, G. A., et al. (2004), CHAMP and SAC-C atmospheric occultation results and intercomparisons, *J. Geophys. Res.*, *109*, D06109, doi:10.1029/2003JD003909.

Healy, S. (2001), Radio occultation bending angle and impact parameter errors caused by horizontal refractive index gradients in the troposphere: A simulation study, *J. Geophys. Res.*, *106*(D11), 11,875–11,890.

Heise, S., J. Wickert, G. Beyerle, T. Schmidt, and C. Reigber (2005), Global monitoring of tropospheric water vapor with GPS radio occultation aboard CHAMP, *Adv. Space Res.*, doi:10.1016/j.asr.2005.06.066.

Jensen, A. S., M. S. Lohmann, H.-H. Benzon, and A. S. Nielsen (2003), Full spectrum inversion of radio occultation signals, *Radio Sci.*, *38*(3), 1040, doi:10.1029/2002RS002763.

Kaplan, E. D. (1996), *Understanding GPS: Principles and applications*, Artech House, Boston, London.

Kuo, Y.-H., T.-K. Wee, S. Sokolovskiy, C. Rocken, W. Schreiner, D. Hunt, and R. A. Anthes (2004), Inversion and error estimation of GPS radio occultation data, *J. Meteorol. Soc. Jpn.*, *82*(1B), 507–531.

Kursinski, E., and G. Hajj (2001), A comparison of water vapor derived from GPS occultations and global weather analyses, *J. Geophys. Res.*, *106*(D1), 1113–1138.

Kursinski, E. R., G. A. Hajj, J. T. Schofield, R. P. Linfield, and K. R. Hardy (1997), Observing Earth's atmosphere with radio occultation measurements using Global Positioning System, *J. Geophys. Res.*, *19*(D19), 23,429–23,465.

Kursinski, E. R., G. A. Hajj, S. S. Leroy, and B. Herman (2000), The GPS radio occultation technique, *Terrestrial, Atmospheric and Oceanic Sciences*, *11*(1), 53–114.

Leiterer, U., H. Dier, and T. Naebert (1997), Improvements in radiosonde humidity profiles using RS80/RS90 radiosondes of Vaisala, *Beitr. Phys. Atmos.*, *70*(4), 319–336.

Marquardt, C., K. Labitzke, C. Reigber, T. Schmidt, and J. Wickert (2001), An assessment of the quality of GPS/MET radio limb soundings during February 1997, *Phys. Chem. Earth, Part A: Solid Earth and Geodesy*, *26*(3), 125–130.

Marquardt, C., K. Schöllhammer, G. Beyerle, T. Schmidt, J. Wickert, and C. Reigber (2003), Validation and data quality of CHAMP radio occultation data, in *First CHAMP mission results for gravity, magnetic and atmospheric studies*, edited by C. Reigber, H. Lühr, and P. Schwintzer, pp. 384–396, Springer–Verlag, Berlin.

Melbourne, W. G., E. S. Davis, C. B. Duncan, G. A. Hajj, K. R. Hardy, E. R. Kursinski, T. K. Meehan, L. E. Young, and T. P. Yunck (1994), The application of spaceborne GPS to atmospheric limb sounding and global change monitoring, *JPL Publication 94-18*, Jet Propulsion Laboratory, Pasadena, CA, USA.

Misra, P., and P. Enge (2002), *Global positioning system: Signals, measurements, and Performance*, Navtech Seminars and GPS Supply, Suite 400, 6121 Lincolnia Rd., Alexandria, VA, USA.

Reigber, C., H. Lühr, and P. Schwintzer (2002), CHAMP mission status, *Adv. Space Res.*, *30*(2), 129–134.

Reigber, C., H. Lühr, P. Schwintzer, and J. Wickert (2005), *Earth Observation with CHAMP: Results from Three Years in Orbit*, Springer–Verlag, Berlin Heidelberg New York.

Rocken, C., et al. (1997), Analysis and validation of GPS/MET data in the neutral atmosphere, *J. Geophys. Res.*, *102*(D25), 29,849–29,866.

Sokolovskiy, S. (2004), Open loop tracking and inverting GPS radio occultation signals: Simulation study, in *Occultations for probing atmosphere and climate*, edited by G. Kirchengast, U. Foelsche, and A. K. Steiner, pp. 39–51, Springer–Verlag, Berlin.

Sokolovskiy, S., C. Rocken, D. Hunt, W. Schreiner, J. Johnson, D. Masters, and S. Esterhuizen (2005), Inversion of open-loop radio occultation sig-

nals at CDAAC, Second GPS Radio Occultation Data Users Workshop, National Conference Center, Lansdowne, VA, USA, presentation available at http://www.cosmic.ucar.edu/gpsro2/presentations/Sokolovskiy_GPSRO_2005.pdf.

Sokolovskiy, S. V. (2001), Tracking tropospheric radio occultation signals from low Earth orbit, *Radio Sci.*, *36*(3), 483–498.

Sokolovskiy, S. V. (2003), Effect of superrefraction on inversions of radio occultation signals in the lower troposphere, *Radio Sci.*, *38*(3), 1058, doi:10.1029/2002RS002728.

Stephens, S. A., and J. B. Thomas (1995), Controlled-root formulation for digital phase-locked loops, *IEEE Transactions on Aerospace and Electronic Systems*, *31*(1), 78–95.

Syndergaard, S. (2000), On the ionosphere calibration in GPS radio occultation measurements, *Radio Sci.*, *35*(3), 865–884.

Thomas, J. B. (1989), An analysis of digital phase-locked loops, *JPL Publication 89-2*, Jet Propulsion Laboratory, Pasadena, USA.

Tsui, J. B.-Y. (2000), *Fundamentals of Global Positioning System Receivers: A Software Approach*, 258 pp., John Wiley & Sons, Inc., New York.

Vaisala (1989), Upper air systems: RS80 radiosondes, *Tech. rep.*, Vaisala GmbH, Hamburg.

von Engeln, A., G. Nedoluha, and J. Teixeira (2003), An analysis of the frequency and distribution of ducting events in simulated radio occultation measurements based on ECMWF fields, *J. Geophys. Res.*, *108*(D21), 4669, doi:10.1029/2002JD003170.

von Engeln, A., J. Teixeira, and G. Beyerle (2005), The impact of thin water vapor layers on CHAMP radio occultation measurements, *Radio Sci.*, submitted.

Wickert, J., T. Schmidt, G. Beyerle, R. König, C. Reigber, and N. Jakowski (2004), The radio occultation experiment aboard CHAMP: Operational data analysis and validation of atmospheric profiles, *J. Meteorol. Soc. Jpn.*, *82*(1B), 381–395.

Wickert, J., et al. (2001), Atmosphere sounding by GPS radio occultation: First results from CHAMP, *Geophys. Res. Lett.*, *28*(17), 3263–3266.

Yunck, T. P., C.-H. Liu, and R. Ware (2000), A history of GPS sounding, *Terrestrial, Atmospheric and Oceanic Sciences*, *11*(1), 1–20.

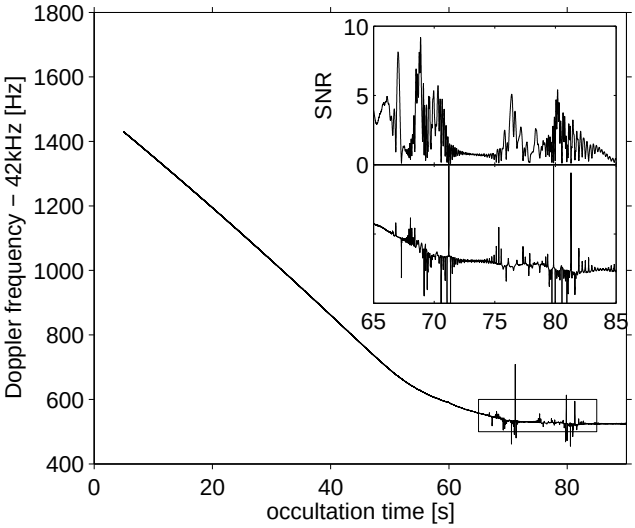


**Figure 1.** Simulated Doppler frequency profile derived from a radio sonde observation at 29.9°N, 14.6°W on 2 January 1983 (simulation run #10). The insert shows the Doppler profile within the multipath zone (bottom) together with the corresponding voltage signal-to-noise ratio (top).

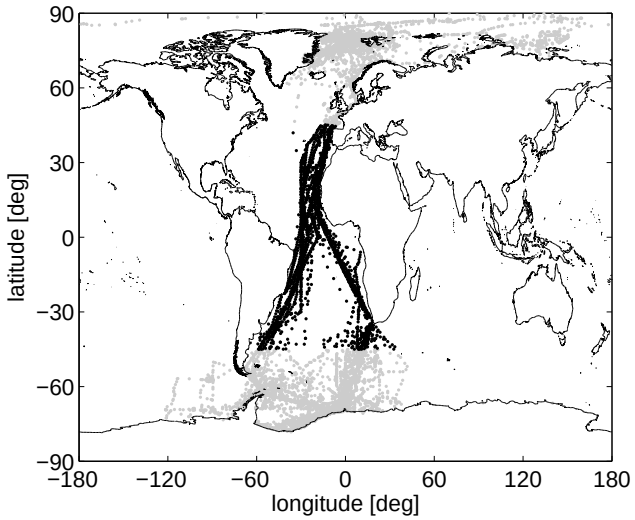


**Figure 2.** Map of aerological soundings performed aboard research vessel "POLARSTERN" between December 1982 and June 2005 (grey dots). The present analysis is focused on 1992 sonde observations recorded between 45°S and 45°N (black dots).

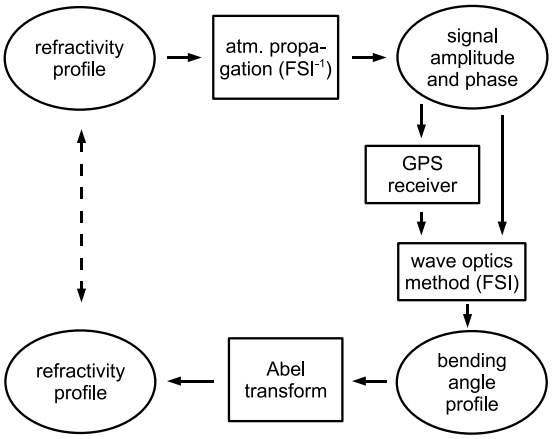


**Figure 3.** Schematic overview of the end-to-end simulation procedure. Using the inverse FSI method the atmospheric propagation of a GPS signal based on a refractivity profile is modelled. The signal is converted to a bending angle profile; its Abel-transformation yields the retrieved refractivity profile closing the simulation loop. Optionally, a GPS receiver model is inserted into the simulation chain.

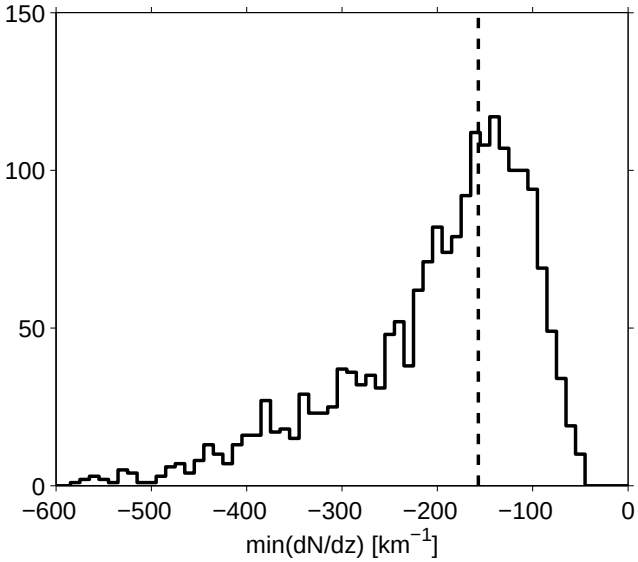


**Figure 4.** Histogram distribution of the minimum of the vertical refractivity gradient, $dN(z)/dz$. The dashed line marks the threshold value for critical refraction $dN_c(z)/dz = -157$ km$^{-1}$.

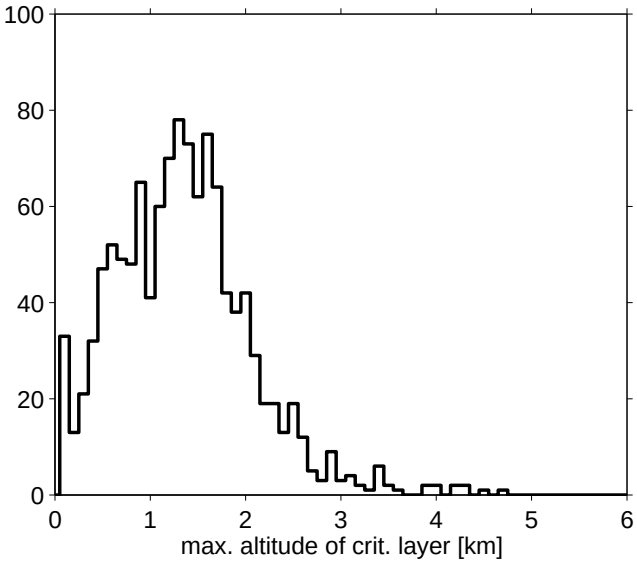


**Figure 5.** Histogram distribution of the highest altitude at which refractivity gradients below the critical threshold value are found.

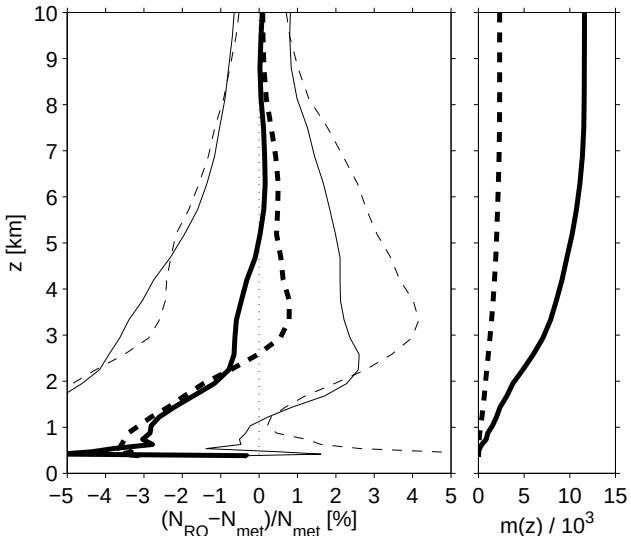


**Figure 6.** Left: fractional refractivity deviation between CHAMP refractivity $N_{RO}$ and ECMWF analyses $N_{met}$ restricted to a subset of 11,626 observations over the Atlantic (full line). The dashed line marks the corresponding result derived from 2336 occultation events over the Amazon region. The corresponding one-sigma standard deviations are plotted as thin lines. Right: number of observed refractivity data as a function of altitude. The loss-of-lock altitudes are $z_{50\%} = 2.5$ (Atlantic) and 2.8 km (Amazon region), respectively.

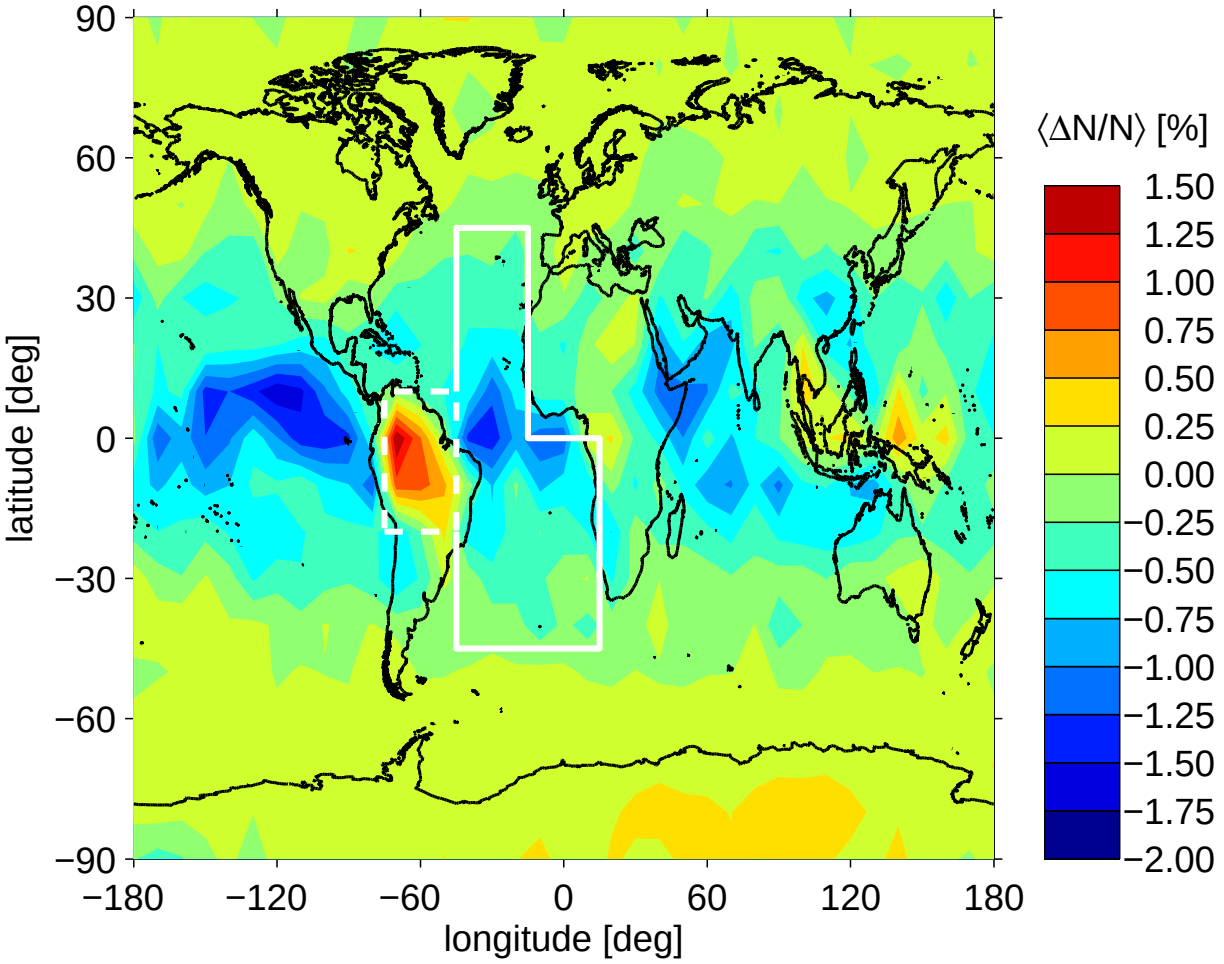


**Figure 7.** Global map of fractional refractivity deviation between CHAMP observations and corresponding ECMWF analyses. The mean deviations between 3 and 5 km altitude are calculated from 206,422 profiles sorted into $10° \times 10°$ longitude/latitude bins. White lines mark the regions of the two subsets plotted in Fig. 6.

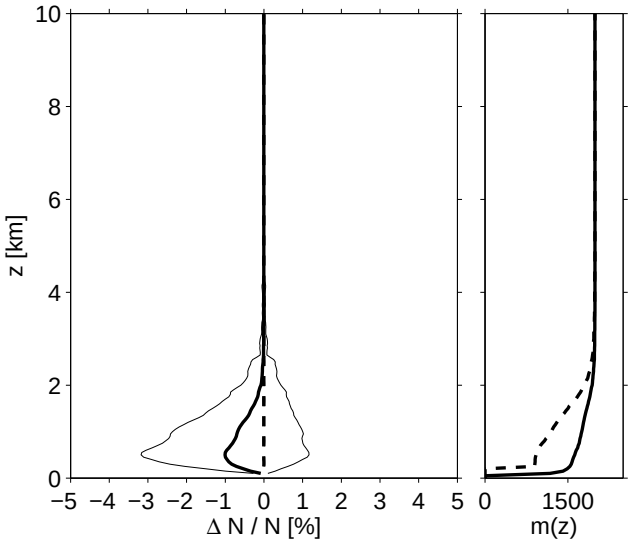


**Figure 8.** Left: fractional refractivity error derived from simulations using the ideal receiver (model A) is plotted as thick solid line. The thin lines indicate the one-sigma standard deviation. Excluding data affected by critical refraction yields an almost bias-free result (dashed lines) with a standard deviation of less than 0.03%. Right: number of retrieved data points. $z_{50\%}$ are 692 m and 99.5 m, respectively.

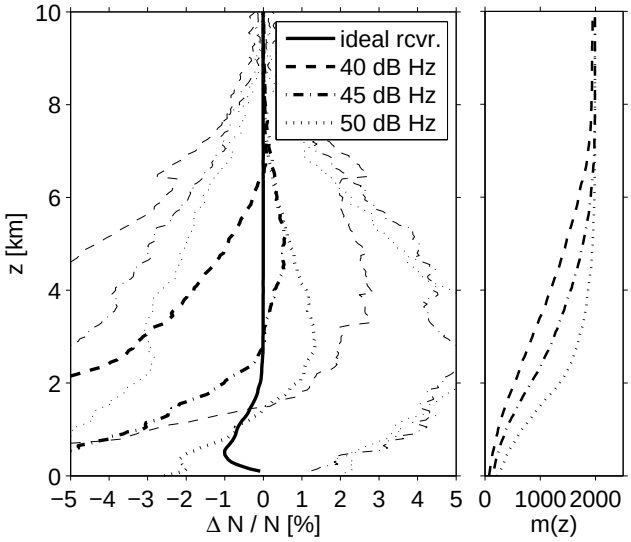


**Figure 9.** Same as Fig. 8, however signal is tracked in closed-loop mode with fly-wheeling enabled (model B). $z_{50\%}$ are 3.4, 2.3 and 1.5 km for 40, 45 and 50 dB Hz, respectively. The full line (left panel) marks the ideal receiver ('ideal rcvr.') result (Fig. 8).

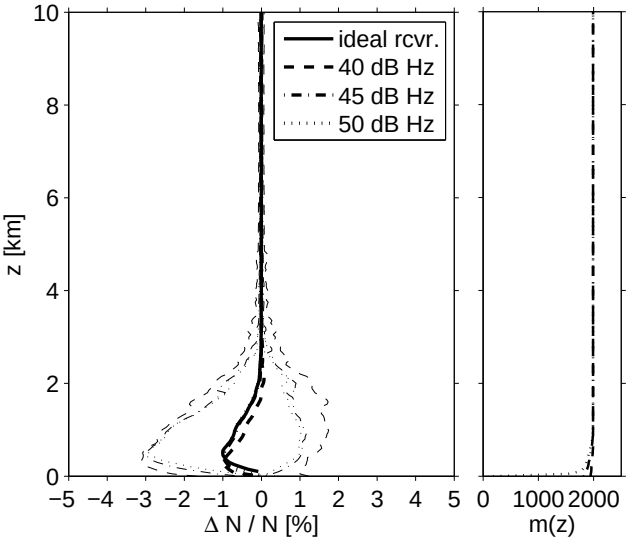


**Figure 10.** Same as Fig. 8, however signal is tracked in open-loop mode (model C). $z_{50\%}$ is 0.023 km for 50 dB Hz. At 40 dB Hz and 45 dB Hz the number of retrieved data points exceeds 50% at all heights rendering $z_{50\%}$ undefined.

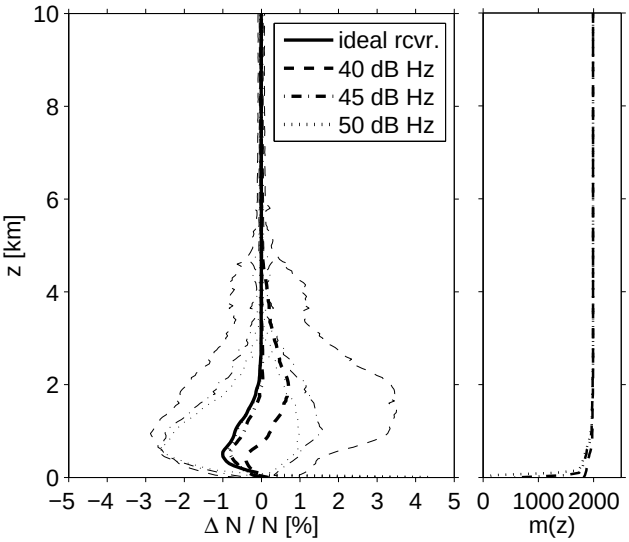


**Figure 11.** Same as Fig. 10, however Doppler frequency model is shifted by +10 Hz. $z_{50\%}$ are 0.023 and 0.086 km for 45 and 50 dB Hz.

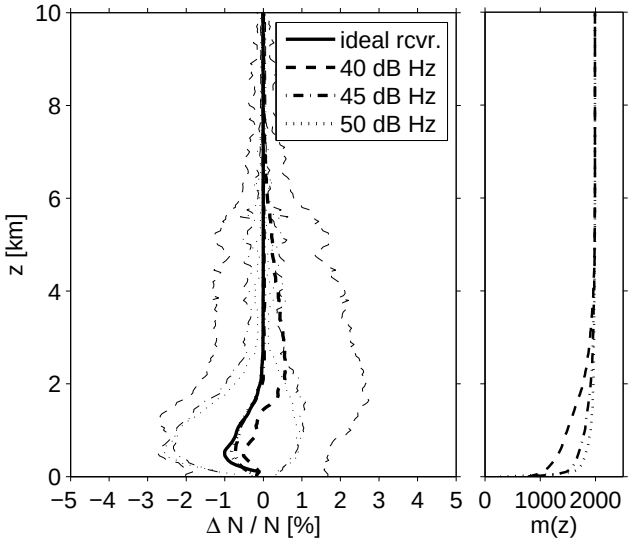


**Figure 12.** Same as Fig. 8, however signal is tracked in closed-loop mode with carrier loop bandwidth reduced to 5 Hz (model D). $z_{50\%}$ are 0.11, 0.025 and 0.039 km for 40, 45 and 50 dB Hz, respectively.

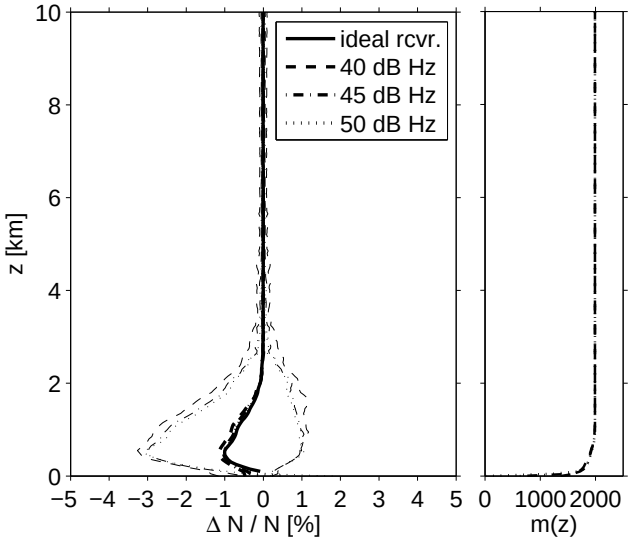


**Figure 13.** Same as Fig. 8, however signal is tracked in closed-loop mode with second order loop (model E). $z_{50\%}$ are 0.019 and 0.040 km for 45 and 50 dB Hz, respectively.

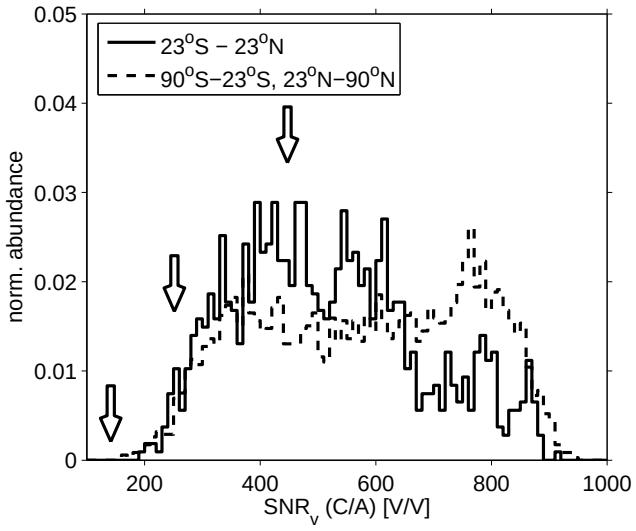


**Figure 14.** Normalized occurrence distribution of L1 C/A voltage signal-to-noise ratios derived from January 2004 CHAMP occultation data in the Tropics (solid line) and at mid/high latitude (dashed). Each distribution is normalized to the corresponding total number of events, which are 1073 and 3453 observations, respectively. The signal-to-noise ratios are extracted from the profiles' initial, unattenuated sections. The arrows mark the signal-to-noise density ratios of 40, 45 and 50 dB Hz.

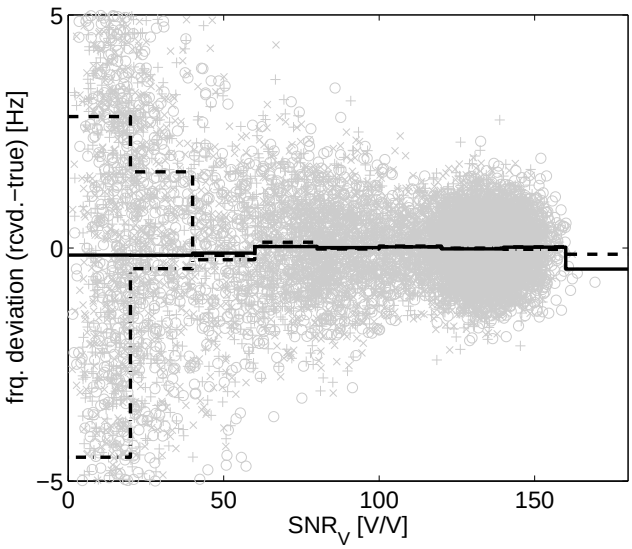


**Figure 15.** Deviation between retrieved and true frequency as a function of voltage signal-to-noise ratio at $C/N_0 = 40$ dB Hz extracted from simulation run #10 (Fig. 1). The signal is tracked in open-loop mode with Doppler model shifted by +10, 0 and −10 Hz. The corresponding frequency deviations averaged over bins of width 10 V/V are plotted as dashed, solid and dashed-dotted lines, respectively; the individual data points are marked in grey.

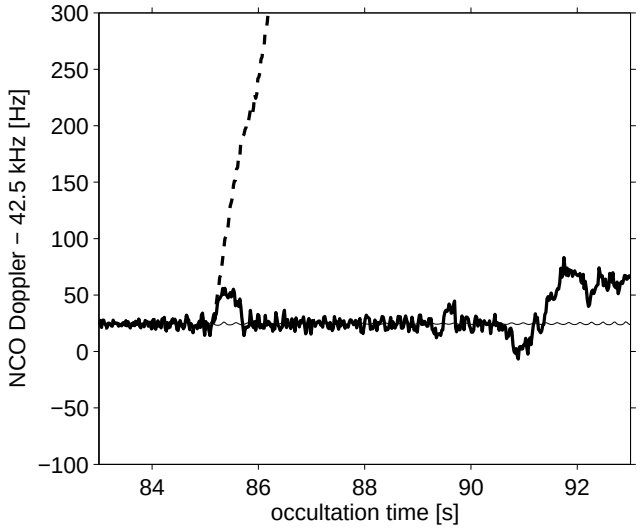


**Figure 16.** NCO Doppler frequency for second order (solid) and third order (dashed) closed-loop tracking as a function of occultation time. The second order loop experience loss-of-lock at 90.5 s occultation time, the third order loop already at 85.2 s. The thin line marks the true Doppler profile. An offset of 42.5 kHz is subtracted for clarity.

**Table 1.** Characteristics of the five receiver models used in the simulations.

| receiver model | tracking | loop bandwidth | loop order | phase extraction | comments |
|---|---|---|---|---|---|
| A | no | | | | ideal receiver |
| B | closed-loop / fly-wheeling | 30 Hz | 3 | 2-quadrant | "CHAMP-like" |
| C | open-loop | | | 4-quadrant | |
| D | closed-loop | 5 Hz | 3 | 4-quadrant | |
| E | closed-loop | 30 Hz | 2 | 4-quadrant | |